Graph-based analysis of kinetics on multidimensional potential-energy surfaces

T. Okushima,* T. Niiyama, K. S. Ikeda, and Y. Shimizu
Department of Physics, Ritsumeikan University, Noji-higashi 1-1-1, Kusatsu 525-8577, Japan
(Received 17 December 2008; revised manuscript received 16 April 2009; published 17 September 2009)

The aim of this paper is twofold: one is to give a detailed description of an alternative graph-based analysis method, which we call *saddle connectivity graph*, for analyzing the global topography and the dynamical properties of many-dimensional potential-energy landscapes and the other is to give examples of applications of this method in the analysis of the kinetics of realistic systems. A Dijkstra-type shortest path algorithm is proposed to extract dynamically dominant transition pathways by kinetically defining transition costs. The applicability of this approach is first confirmed by an illustrative example of a low-dimensional random potential. We then show that a coarse-graining procedure tailored for saddle connectivity graphs can be used to obtain the kinetic properties of 13- and 38-atom Lennard-Jones clusters. The coarse-graining method not only reduces the complexity of the graphs, but also, with iterative use, reveals a self-similar hierarchical structure in these clusters. We also propose that the self-similarity is common to many-atom Lennard-Jones clusters.

DOI: 10.1103/PhysRevE.80.036112 PACS number(s): 89.75.Hc, 31.50.−x

I. INTRODUCTION

In recent years, the variety of structural, thermodynamic, and dynamical phenomena observed in simulations and experiments of a wide range of systems, such as polyatomic clusters [1–4], carbon nanostructures [5,6], biomolecules [7,8], and glass-forming materials [9–20], have been attributed to the complicated geometry of the underlying potential-energy surfaces (PESs) [21,22].

When a PES is a many-dimensional surface, it is hard to visualize and analyze its global geometric character. For analyzing the global topography of PES, several graphical representations have been developed. One of the most popular methods is the *disconnectivity graph* (DG), proposed by Becker and Karplus in 1997 [7]. This graph depicts the disconnectivity, i.e., how basins split up into sub-basins as the total energy of the system is lowered. By using this simple and popular method, for example, structural transitions of clusters and archetypal classification of PESs associated with relaxation characteristics can be intuitively represented and analyzed [22].

The relation between the topographies of PESs and the resulting dynamical properties, such as the folding dynamics of biomolecules, are of much recent interest. Several graph methods, such as the basin connectivity graph [7], the transition matrix [7], the monotonic sequence plot of minima [1], and the supergraph [23,24], have been devised to extract the qualitative features of kinetics. With these methods, kinetic features, such as the criterion for the (anti)focusing character of the PESs [1], the competitions of fast pathways for rates depending on the temperature [25], and the formation of kinetic traps on PESs [1], have been elucidated from topographical views. However, when they are applied to realistic multidimensional systems, the graphs are too complex as they are. Coarse-graining procedures have been used to extract some essential features [22]. However, understanding the relation between the topography and dynamics is still difficult due to the complexity resulting from the multidimensionality. Therefore, a better topographic representation is required for the understanding of global PES dynamics.

Recently, we have proposed an alternative graph method, saddle connectivity graph (SCG), which was called "connectivity graph" for short in our previous paper [26]. The SCG is a graph method for analyzing the dynamical properties on PESs and is regarded as a generalization of the DG to include global dynamical information. With this graph method, we can, for example, identify which pathways are dominant for the transitions between potential minima. In Ref. [26], we devised a systematic method for finding the most dominant transition pathways, a natural generalization of the so-called minimum-energy paths [22]. This method is applicable when the relaxation in each well is fast enough for the transitions to be described by Rice-Ramsperger-Kassel-Marcus (RRKM) rate theory [22]. We introduced a metric (cost or distance) to characterize transition paths for passing from a minimum to another neighboring minimum to identify the most dominant pathways. The most dominant pathways of interest are easily computed with the help of Dijkstra's shortest path algorithm [27] in the field of graph theory.

Of course, the problem of the huge number of local minima, which is well known in the use of DGs, was also found for the SCG. To evade this difficulty, a coarse-graining method, based on the monotonic sequence method [1,28,29], was proposed for our SCG [26]. This method enables us not only to reduce the complexity of the graphs, but also to extract the hierarchical structures.

This method is general, efficient, and applicable to a vast variety of systems. The purpose of the paper is twofold: one is to give a detailed description of the algorithms and the other purpose is to advance, with the use of our graphic approach, the understanding of the dynamical properties on realistic multidimensional PESs. For this end, we analyze 13- and 38-atom Lennard-Jones (LJ) clusters, as paradigmatic multidimensional model systems and compare how the dominant pathways of the systems are altered by changing their temperatures.

The organization of the paper is as follows. In Sec. II, after introducing the DG, we describe the detailed algorithm

*okushima@ike-dyn.ritsumei.ac.jp

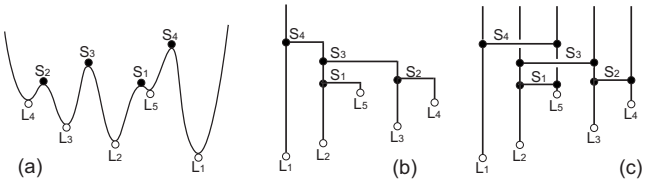

FIG. 1. (a) A schematic of one-dimensional potential energy with five local minima $L_1, L_2, \ldots, L_5$ and four saddle points S_1, S_2, S_3, S_4, indicated by white and black circles, respectively. The corresponding DG and SCG are shown in (b) and (c), respectively.

for generating SCGs. Section III introduces an illustrative example, which we call a random funnel model (RFM), and illustrates how the SCG works for this model. In Sec. IV, we describe a systematic procedure for finding pathways that contribute most dominantly to the transport on PESs, with the help of Dijkstra's shortest path algorithm. Section V describes the coarse-graining method for SCGs, which has been invented to treat realistic systems. In Sec. VI, with the use of all these methods, we examine the dominant pathways of many-atom Lennard-Jones clusters. Section VII provides a summary of the paper and concluding remarks.

II. SADDLE CONNECTIVITY GRAPH

After reviewing the DG, we describe the procedure for generating the SCG. The difference between disconnective and nondisconnective saddles is introduced. A generalization of SCG to include higher-order saddles, as well as first-order ordinary saddles, is also presented.

A. Disconnectivity graph

Since the work by Becker and Karplus [7], the DG has been widely used to analyze the topography of PESs. A PES is partitioned into the basins of the local minima (local minima, LMs) corresponding to the stable configurations, where all the eigenvalues of Hessian matrices are positive. The boundaries of basins are characterized by the saddle points (SPs). Each SP has a negative eigenvalue of Hessian matrix and the energy of the SP determines the connectivity between the adjacent LMs.

The DG is a topological representation that represents how a single metabasin is decomposed into basins by lowering the total energy. From the DG, we can know the number of energetically accessible metabasins and the LMs included in each metabasin as a function of the total energy. These indeed provide information to estimate the *static* thermodynamic properties [7,22]. However, the DG does not provide the information about pathways on the PES.

Figure 1(a) is a schematic example of one-dimensional (1D) PES illustrating this point. From the corresponding DG of Fig. 1(b), we cannot see that L_1 and L_5 are neighbors separated by only one SP. However, the undepicted information of how many hops over SPs are necessary to travel from one LM to another is, in principle, indispensable to evaluate the *dynamic* properties on the PES.

B. Saddle connectivity graph

Now we describe the procedure of how to draw the SCG from a given PES. For the graph, we have to construct the database of LMs, SPs, and their saddle connectivity. The LMs are easily located by geometry optimization schemes, such as steepest-descent minimization, conjugate-gradient method, limited memory Broyden-Fletcher-Goldfarb-Shanno (L-BFGS) algorithm, and their hybrid algorithms [22].

In contrast, finding SPs is in general more difficult and many algorithms for this purpose have been developed. These are classified into single-ended and double-ended methods. Many single-ended schemes, such as the eigenvector-following method, the hybrid eigenvector following with minimization [22,30], and the dimer method [31], have been constructed for searching for a SP from a given initial point on the PES. On the other hand, the double-ended methods, such as nudged elastic band approach [32], enable us to calculate a reaction path that connects two arbitrary LMs, which may include intermediate minima and additional transition states [22].

The saddle connectivity is also necessary for the SCG database. This is computed by energy minimizations starting from two neighboring points in the unstable direction on opposite sides of each SP by using, for example, steepest-descent algorithm.

The resulting database obtained from the above procedure is composed of three parts:

(1) the set of LMs $\{L_i | i=1,2,\ldots,M\}$ of energies $E_i^{\mathrm{LM}} = V(L_i)$, where M is the number of LMs and V is the potential-energy function;

(2) the set of SPs $\{S_i | i=1,2,\ldots,N\}$ of energies $E_i^{\mathrm{SP}} = V(S_i)$, where N is the number of SPs; and

(3) the saddle connectivity of S_j $(j=1,2,\ldots,N)$, which connect L_{j_1} and L_{j_2} $(j_1, j_2 = 1,2,\ldots,M)$. This relation is represented by

$$g(S_j) = \{j_1, j_2\} \quad (j_1 < j_2), \tag{1}$$

where E_i^{LM} and E_i^{SP} are, respectively, assumed to be sorted in an increasing order, without loss of generality.

In the SCG, LMs are represented by half vertical lines from E_i^{LM} to ∞. For representing the individual saddle connectivity, S_j is indicated by a horizontal segment attached to the vertical LM lines of $g(S_j)$. Then, the lines of LMs are placed at even intervals in the order $L_{\sigma(1)}, L_{\sigma(2)}, \ldots, L_{\sigma(M)}$, where permutation σ is defined in order not to loose the information of disconnectivity. We specify σ by using a *metabasin analysis* as follows:

(1) Initialize the ordered set of ordered sets, R, as

$$R = \{\{1\},\{2\},\ldots,\{M\}\}.$$

(2) Repeat the following step from $i=1$ to N: if S_i connects two elements of R (say, R_a and R_b with $a<b$), i.e.,

$$R_a \cap g(S_i) \neq \phi, \quad R_b \cap g(S_i) \neq \phi, \tag{2}$$

then unite them by appending elements of R_b to R_a. This merging procedure stops properly when R has only one element, i.e., $R=\{R_1\}$.

(3) Finally, σ is given by $\sigma = R_1$.

The resulting σ is normalized such that the global minimum (GM) of L_1 is placed on the extreme left, i.e., $\sigma(1)=1$. Note that if R otherwise has more than two elements at the end of the procedure, then the LMs are disconnected by the SP linkages listed in the present database. In this case, we have to redefine the total set of LMs as the first element of R including the GM, and the resulting saddle connections are restricted to be between them. Otherwise, we have to go back to the database construction and enhance its completeness [33].

For example, the metabasin analysis for the one-dimensional potential depicted in Fig. 1(a) proceeds as follows:

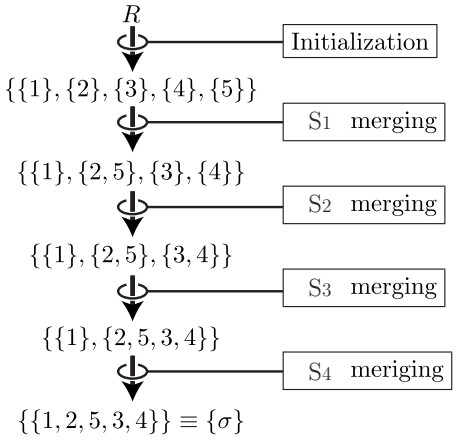

By using the resulting order $\sigma=\{1,2,5,3,4\}$, we depict the SCG for this example in Fig. 1(c). By comparison with the DG of Fig. 1(b), it can be seen that the SCG shows the disconnectivity of the schematic PES. The more important feature is that, as expected, the SCG represents the direct connection between L_1 and L_5 by a single horizontal segment connecting two vertical lines drawn from points 1 and 5.

C. Disconnective and nondisconnective saddles

In order to show the difference between DGs and SCGs, we classify saddles into two types: *disconnective saddles* (DSs) and *nondisconnective saddles* (NDSs). When the total energy of the system is lowered below the potential energy of a certain DS, the basin that is connected by the DS splits up into two basins. In contrast to this, in the vicinity of the energy of a NDS, there is no decomposition of basin resulting from the NDS. Hence, the DSs represent the *energetically cheapest* pathways to travel. The NDSs are more expensive but *can be dynamically dominant* pathways between some two minima. Note here that, in the course of the metabasin analysis described in Sec. II B, saddles are classified to be DSs if Eqs. (2) are satisfied; otherwise, they are classified to be NDSs. It should be emphasized that the SCG represents both the DSs and the NDSs, while the DG does not represent the NDSs.

D. Higher-order saddles in SCG

Here, we generalize SCGs to represent higher-order saddles. A higher-order saddle is a stationary point with more than one negative eigenvalue of the Hessian matrix, and the order of saddle is the number of the negative eigenvalues. Higher-order saddles can connect more than two LMs. Figure 2(a) illustrates this point: a second-order saddle S_4 connects three LMs of L_1, L_2, and L_3.

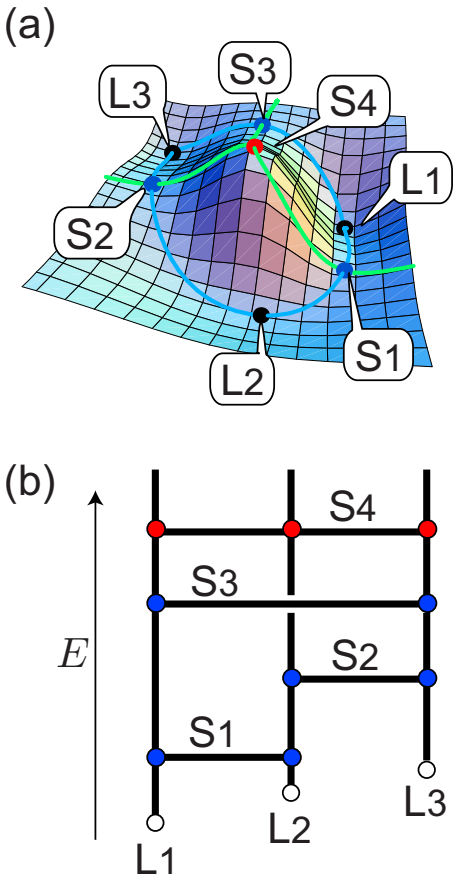

FIG. 2. (Color online) (a) A schematic of 2D PES having three local minima L_1, L_2, L_3 and four saddle points, where S_1, S_2, S_3 are first-order and S_4 is a second-order SP, i.e., maximum in the 2D configurational phase space. (b) The corresponding SCG is depicted. Note that S_4 is represented by a horizontal line with three contact points (see text).

As shown in Fig. 2(b), S_4 is represented by a horizontal segment with three contact points that are joined to the vertical lines of these LMs at the saddle-energy level, in the corresponding SCG. This expressiveness is another advantage of SCG over other graph methods.

Note that the possibility that these higher-order saddles play an important role for the relaxation dynamics has been discussed in, e.g., Refs. [34,35]. In the following, however, we will focus on ordinary first-order saddle points in SCG, for the sake of the comparison with the other popular graph methods.

III. RANDOM FUNNEL MODEL

A visually comprehensive example would be suited for examining how the SCG works for realistic problems. Hence, in this section, we introduce a certain type of random model potential, which we refer to as a RFM. This model is

not only simply illustrative, but also is able to represent a funnel structure, which has been widely discussed as a key factor for fast protein folding dynamics in kinetic approach. In the following, we show that, with the help of SCG visualization, the RFM changes from multifunnel, through single funnel, to smooth funnel feature by increasing its funnel inclination parameter.

In order to ensure spatial periodicity of the RFM, we employ the following procedure to construct the PES. The 1D RFM potential $V(x)$ is a convolution of a Gaussian kernel, standard deviation σ,

$$G(x) = \frac{1}{\sqrt{2\pi}\sigma} e^{-x^2/2\sigma^2}, \tag{3}$$

with distribution $\rho(x)$ that is a sum of delta functions

$$\rho(x) = \sum_{n=-\infty}^{\infty} \sum_{j=1}^{L} A_j \delta(x - j - nL), \tag{4}$$

where the periodic boundary condition is imposed on the interval $(0, L]$ and the amplitudes A_j are randomly sampled from the uniform distribution on the interval of $U(n) < A_n < U(n)+1$, with a prototype function U. The prototype function $U(x)$ is chosen as a funnel-shaped function

$$U(x) = \frac{2F|x - L/2|}{L}$$

with funnel inclination parameter F. Lastly, for computational simplicity, $V(x)$ is low-pass filtered with the reciprocal wave number π of the lattice. The Fourier-based actual computation for $V(\mathbf{x})$ is described in Appendix A.

Next we introduce the d-dimensional RFM potential $V(x_1, x_2, \ldots, x_d) \equiv V(\mathbf{x})$, which is similarly constructed by the convolution of the Gaussian kernel

$$\frac{1}{(\sqrt{2\pi}\sigma)^d} \exp\left(- \frac{\sum_{i=1}^{d} x_i^2}{2\sigma^2} \right)$$

with the delta-function potential located at integer points $\mathbf{x} = \mathbf{j}$ $(1 \le j_1, j_2, \ldots, j_d \le L)$. The delta-function amplitudes $A_{\mathbf{j}}$ are sampled from the uniform distribution on the interval from $U(\mathbf{j})$ to $U(\mathbf{j})+1$ with a d-dimensional funnel-shaped function of funnel depth F,

$$U(\mathbf{x}) = \frac{2F \max_{1 \le i \le d} \{|x_i - L/2|\}}{L}. \tag{5}$$

Then the periodic boundary condition is imposed on the d-dimensional unit square $D \equiv (0, L]^d$. In actual computation, $V(\mathbf{x})$ is also efficiently evaluated via Fourier-based procedures, as described in Appendix A.

Here, we examine the two-dimensional (2D) RFM. The left panels of Fig. 3 show the contour plots of 2D RFMs for $F=0$, 0.4, 0.8, 1.2, and 2.4 with an identical seed of the random number generator. These figures elucidate that a larger F yields a smoother funnel-shaped PES. The configuration space of the RFM of $F=0$ in Fig. 3(a) is divided into multiple LM basins of approximately equal areas. When F becomes larger, however, the GM near the center $(x, y) = (8, 8)$ sinks and its basin becomes dominating, as clearly shown in Figs. 3(b) and 3(c). For larger F, the funnel character gradually becomes apparent, as typically shown in Figs. 3(d) and 3(e), where the GM becomes deeper and some LMs at $F=0$ disappear.

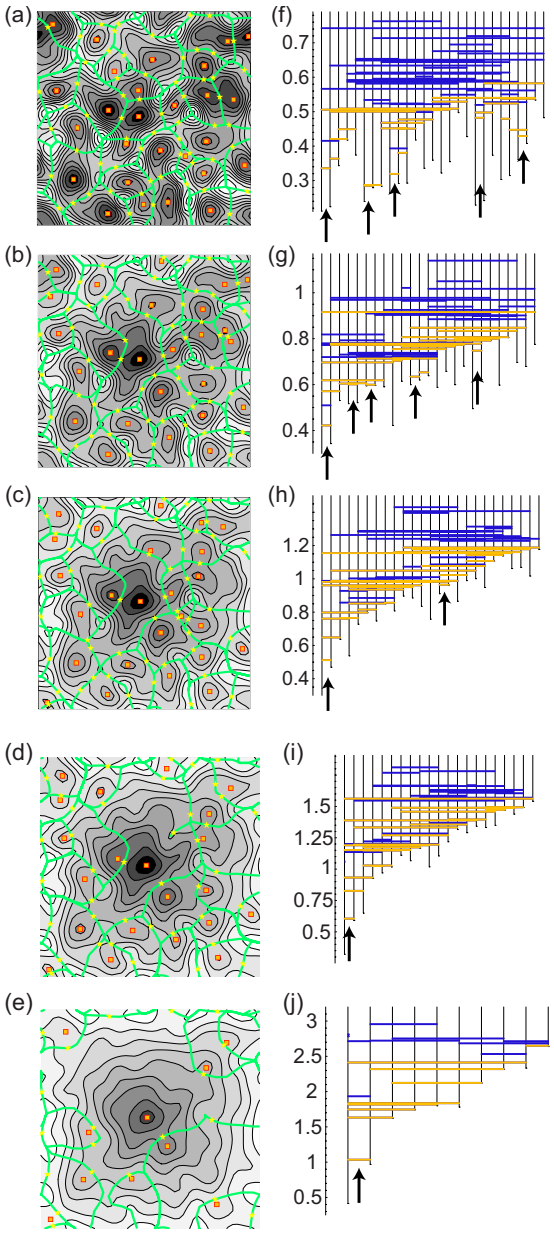

FIG. 3. (Color online) Left panels: contour plots of two-dimensional RFMs with $L=16$ and $\sigma=0.73$ for $F=0$, 0.4, 0.8, 1.2, and 2.4 are shown in (a), (b), (c), (d), and (e), respectively. The LMs (boxes), the SPs (stars), and the boundaries of the LM basins [green (light-gray) lines] are also depicted. Right panels: The SCGs corresponding to the left panels are presented in (f)–(j) with the vertical axes of potential energy. Here, the orange (light-gray) and the blue (dark-gray) lines denote the pathways which run through DSs and NDSs, respectively. In (f)–(h), for eye guidance, arrows, which indicate the bottoms of funnels contained in the potentials, are shown.

Let us examine how these RFMs are represented in the corresponding SCGs. The right panels of Fig. 3 are the SCGs corresponding to the contour plots in the left sides, respectively.

First, as shown in panels (f)–(h), the PESs of small F are composed of multiple funnels. Each funnel contains multiple LMs and SPs. The SP with lowest energy in each funnel is indicated with an arrow. These bottoms are relevant for, for example, the Markovian hopping dynamics, because the back-and-forth motions over these saddles are very frequent and thus there can appear kinematic traps, as discussed in Ref. [16]. Note that the decrease in the number of the funnels with increasing F is apparent in the SCGs, while this is not clear in the contour plots.

The SCG of 2D RFM with $F=0$ in Fig. 3(f) shows that the random-energy LM lines are randomly connected, at various saddle energy levels, with $(M-1)$ DS lines (M=the number of LMs) in a relatively low energy region $E^{\mathrm{SP}} \lesssim 0.6$, as well as with many extra NDS lines in a relatively higher $E^{\mathrm{SP}} \gtrsim 0.5$, where some NDSs are coexistent with DSs in $0.4 \lesssim E^{\mathrm{SP}} \lesssim 0.6$. In addition, we see that the PES is composed of five funnels.

The SCG with $F=0.4$ in Fig. 3(g) also exhibits five funnels, while LM energies are not completely random any more. Instead, we see the clear tendency that the more right LM is placed on the horizontal axis, the higher is the energy of the LM. Namely, the higher-energy LM tends to be connected with the GM at higher energy. In this case too, many NDS lines connect many pairs of LMs both in the coexistent and in the higher region.

In contrast to these, the SCG with $F=0.8$ in Fig. 3(h) exhibits two funnels and the tendency of the LM-energy difference from the GM is more apparent. Furthermore, according to the expansion of the GM basin, the number of LMs adjacent to the GM is increased, which is also clear in the corresponding SCG from the many direct links that connect the GM to the surrounding LMs.

The SCG with $F=1.2$ in Fig. 3(i) exhibits a rugged single funnel feature clearly, where each LM has at least one pathway to the GM with monotonically decreasing saddle energies.

A typical SCG for smooth funnel-shaped PES is plotted in Fig. 3(j) for $F=2.4$, where the barrier height of the DS from each LM to the left LM is very low. Now all direct links to the GM from the adjacent LMs become *DS lines*. This suggests that, when a PES is a smooth funnel, the description of DSs becomes a good approximation for low-energy topology, because the contribution of few NDSs to the connectivity is negligible compared to that of DSs (see below). In this section, we have shown that the SCG, by the graph of LMs connected by DSs and NDSs, effectively represents the topography of PES, including the number of funnels and the smoothness and the steepness of funnels.

IV. PATHWAYS IN KINETIC PROCESS

We have seen that DSs and NDSs coexist in energy bands. In low-temperature limit, only the most energetically economical saddles are effective and the dynamics is governed by the least energy principle. However, as the temperature is raised, there is a chance for an energetically expensive NDS to become a segment of most dominant pathways. Our interest in this section is how these dominant pathways are selected at various temperatures. To clarify this, we examine, with the help of the SCGs, the switches of routes of the dominant pathways.

A. Rate constants

The flux-over-population method is a common procedure to evaluate rate constants. According to Ref. [36], an external sink and a source are connected to the domains of L_b and L_a, respectively, to build a nonequilibrium steady-state current J. This nonequilibrium steady state is further subjected to the boundary condition that the density inside the domain of the sink is zero.

Then the corresponding rate $k_{b\leftarrow a}$ of the passage is given by

$$k_{b\leftarrow a} = \frac{J}{\rho} = \tau^{-1}, \tag{6}$$

where ρ is the population inside the domain of the source and τ is the mean first passage time from L_a to L_b.

When the intra-LM dynamics loses its memory so fast as to forget the previous inter-LM hoppings, the inter-LM dynamics is described by the following coupled master equations:

$$\frac{dP_i(t)}{dt} = \sum_{j\neq i} [k_{ij}P_j(t) - k_{ji}P_i(t)] + J_i, \tag{7}$$

$$J = \begin{cases} J & \text{for } i = a \\ -J & \text{for } i = b \\ 0 & \text{for } i \neq a,b, \end{cases} \tag{8}$$

where $P_i(t)$ denotes the occupation probability in L_i at time t and k_{ji} is the rate constant for a direct transition from L_i to an adjacent L_j. In the following, we use the expression of k_{ji} in the canonical RRKM theory, which is summarized in Appendix B.

B. Dominant-path switches

The rate constant is evaluated for an illustrative simple model with the flux-over-population method, where the maximum probability flow pathways switch with varying temperature and the dependency is well described by an approximate expression. Here, we use the four-LM model depicted in Fig. 4(a). From Eq. (7), the flux J from L_4 to L_1 in Fig. 4(a) obeys

$$\frac{dP_1}{dt} = k_3P_2 + k_4P_3 - (k_3 + k_4)P_1 - J,$$

$$\frac{dP_2}{dt} = k_3P_1 + k_1P_3 + k_5P_4 - (k_1 + k_3 + k_5)P_2,$$

$$\frac{dP_3}{dt} = k_4P_1 + k_1P_2 + k_2P_4 - (k_1 + k_2 + k_4)P_3,$$

$$\frac{dP_4}{dt} = k_5 P_2 + k_2 P_3 - (k_2 + k_5) P_4 + J,$$

where k_i is the rate for crossing the saddle S_i ($i = 1, 2, \ldots, 5$).

The stationary flux under the condition that $P_1 = 0$, $P_4 = 1$ is given by

$$P_2 = \frac{k_4 k_5 + k_1 k_5 + k_1 k_2 + k_5 k_2}{k_3(k_4 + k_1 + k_2) + k_4(k_1 + k_5) + k_1(k_5 + k_2) + k_5 k_2}, \tag{9}$$

$$P_3 = \frac{k_1 k_5 + k_3 k_2 + k_1 k_2 + k_5 k_2}{k_3(k_4 + k_1 + k_2) + k_4(k_1 + k_5) + k_1(k_5 + k_2) + k_5 k_2}, \tag{10}$$

$$J = k_3 P_2 + k_4 P_3. \tag{11}$$

Thus, the rate $k_{1\leftarrow 4}$ is given by

$$k_{1\leftarrow 4} = \frac{J}{P_4} = J. \tag{12}$$

Note that this model has four different pathways from L_4 to L_1, namely,

$$\ell_1 : S_3 \leftarrow S_1 \leftarrow S_2,$$

$$\ell_2 : S_4 \leftarrow S_2,$$

$$\ell_3 : S_3 \leftarrow S_5,$$

$$\ell_4 : S_4 \leftarrow S_1 \leftarrow S_5.$$

The flow $j(\ell)$ along pathway ℓ is equal to the minimum of the flows along all the directed segments. Figure 4(b) shows $j(\ell_i)$ as functions of temperature, for $i = 1, 2, 3, 4$. We see that as the temperature is decreased, the maximum flow pathway changes from ℓ_2 to ℓ_1 at around $\beta = 0.5$.

When a maximum flow pathway ℓ sufficiently dominates others, the rate conducted by ℓ is well approximated by the rate of the hypothetical one-dimensional system that is composed only of the elements of ℓ, because other segments of the original system are negligible in this case. As shown in Fig. 4(b), this hypothesis is actually satisfied except near the switching temperature at around $\beta \sim 0.5$. Hence, the rate along ℓ is approximated by

$$\frac{1}{k_\ell} = \frac{1}{k_{i_1,i_0}} + \frac{1}{k_{i_2,i_1}}\frac{k_{i_0,i_1}}{k_{i_1,i_0}} + \frac{1}{k_{i_3,i_2}}\frac{k_{i_1,i_2}}{k_{i_2,i_1}}\frac{k_{i_0,i_1}}{k_{i_1,i_0}} + \cdots + \frac{1}{k_{i_n,i_{n-1}}}\prod_{m=1}^{n-1}\frac{k_{i_{m-1},i_m}}{k_{i_m,i_{m-1}}}, \tag{13}$$

or equivalently,

$$\frac{1}{k_\ell} = \beta h e^{-\beta E^{\mathrm{LM}}_{i_0}} Z_{i_0}(\beta) \sum_{m=1}^{n} \frac{e^{\beta E^{\mathrm{SP}}_{i_m}}}{Z^{\dagger}_{i_m}(\beta)}, \tag{14}$$

where ℓ is a n-step pathway from L_a to L_b,

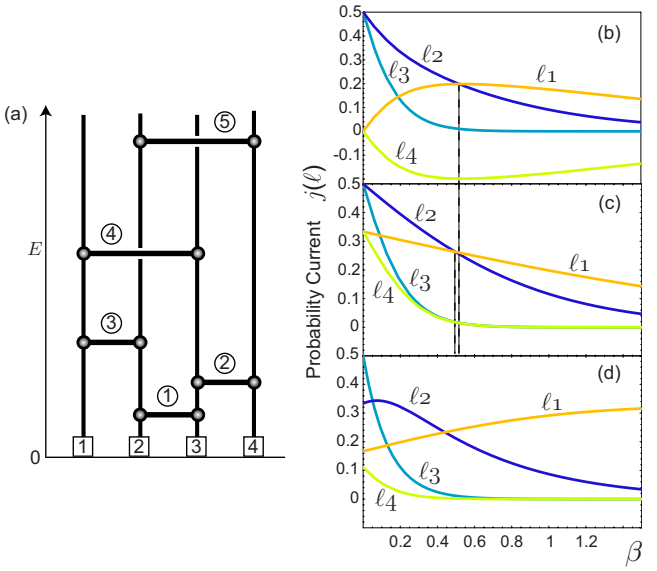

FIG. 4. (Color online) (a) The SCG of a four-LM model. Four LMs of $E^{\mathrm{LM}} = 0$ are connected by five SPs (indicated by circled numbers in the figure). The energies of $S_1, S_2, \ldots, S_5$ are 0.1, 0.2, 1, 2, and 8, respectively. (b) The probability currents from L_4 to L_1 along distinctive pathways, $\ell_1, \ell_2, \ldots, \ell_4$ (see text), are plotted as functions of β. (c) The probability currents calculated via the formula of Eq. (14), are plotted as functions of β. (d) The currents of Eq. (16) are plotted as functions of β, with the same frequency factors. Here, all frequency factors ν_{ji} are set to 1.

$$b \equiv i_n \leftarrow i_{n-1} \leftarrow \cdots \leftarrow i_2 \leftarrow i_1 \leftarrow i_0 \equiv a. \tag{15}$$

See Appendix C for a derivation of Eqs. (13) and (14) and for the definitions of $\beta, Z_i, Z_i^{\dagger}$ in Eq. (14).

By using Eq. (14), we compute the approximate probability fluxes along the paths ℓ_i for the four-LM model of Fig. 4(a). The approximate rates are plotted in Fig. 4(c). Figure 4(c) shows that the probability currents carried by the *most dominant* pathways are well approximated by the approximate rates (14) at all temperatures and that the change in the most dominant pathways is also well described by the same approximations. For degenerate systems, however, slightly different pathways may have approximately equal dominance. In such a case, because it is difficult to detect which one really carries the maximum flow, the switching temperatures calculated by Eq. (14) may give a rough approximation. Even for these degenerate systems, the comparison of Figs. 4(b) and 4(c) supports the conjecture that the approximate formula (14) allows a qualitatively good description of the switches of maximum flux pathways and the order of fluxes along pathways at a given temperature.

Finally, we remark on the difference between Eq. (14) in our use and a similar expression used, for example, in Ref. [37],

$$k_\ell = \frac{k_{b,i_{n-1}} k_{i_{n-1},i_{n-2}} \cdots k_{i_2,i_1}}{\sum_{\alpha_n} k_{\alpha_n,i_{n-1}} \sum_{\alpha_{n-1}} k_{\alpha_{n-1},i_{n-2}} \cdots \sum_{\alpha_2} k_{\alpha_2,i_1}} k_{i_1,a}. \tag{16}$$

As shown in Fig. 4(d), formula (16) does not give a good approximation of the rates along the pathways. It is not sur-

prising because formula (16) computes the hopping rate of sequential process ℓ, while the formula in our use computes an approximate rate of all hopping process, including back-and-forth hoppings along the pathway ℓ. In other words, Eq. (14) is the approximate summation of Eq. (16) over all consecutive hopping processes along ℓ. Note that although formula (16) is useful for efficiently constructing PES databases, because it enables us to extract "fastest pathways" as shown in Ref. [37], it cannot be used to approximate the actual rates carried along the pathways, which are of our interest in this paper. For this end, we should utilize the approximate expression (14).

C. Finding dominant pathways with a Dijkstra shortest path algorithm

By using the above approximate formula (14), we construct a procedure of systematic search for most dominant pathways. The procedure, which is a kind of Dijkstra's shortest path algorithm [27], can be used to find all the dominant pathways coming into a sink from the other LMs in one sweep. This method is very efficient and applicable to high-dimensional PESs.

From Eq. (14), we immediately see that $k_\ell > 0$ for all ℓ and the largest-rate pathway of interest is equivalent to the one with the shortest mean first passage time ($\tau_\ell \equiv k_\ell^{-1}$). Then, Eq. (14) is rewritten as follows:

$$\tau_\ell = (\text{cost along path } \ell) \times [\beta h e^{-\beta E_{i_0}^{\mathrm{LM}}} Z_{i_0}(\beta)], \quad (17)$$

where

$$\text{cost along path } \ell = \sum_{m=1}^{n} C_{\mathrm{pair}}(i_m, i_{m-1}), \quad (18)$$

$$C_{\mathrm{pair}}(i_m, i_{m-1}) = \exp(\beta E_{i_m}^{\mathrm{SP}})/Z_{i_m}^{\dagger}(\beta). \quad (19)$$

Note that $C_{\mathrm{pair}}(i_m, i_{m-1})$ is the positive definite cost of adjacent transition ($i_m \leftarrow i_{m-1}$) and this definition leads to the symmetry $C_{\mathrm{pair}}(i,j) = C_{\mathrm{pair}}(j,i)$. Since the last term in Eq. (17) depends only on the initial LM, i.e., $i_0 = a$, the relevant path contributing most dominantly to $k_{b \leftarrow a}$ is finally characterized by the most inexpensive one that minimizes the route cost (18) with the boundary condition of starting at L_a and ending in L_b.

The point is that the most inexpensive paths of interest are now evaluated methodically by using Dijkstra's shortest path algorithm [27], when the above positive costs are thought of as the distances. In this paper, we use a reverse Dijkstra's algorithm that provides minimum spanning pathways coming into a sink node L_b from all the other nodes, with a slight modification for evading a difficulty coming from the rounding error of floating point computation. The detail of the algorithm is presented in Appendix D.

D. Dominant pathways in 2D RFM

The shortest-path algorithm is applied to the 2D RFMs introduced in Sec. III with several funnel inclination parameters F. By using the SCG visualization, we consider how dominant pathways relevant for rate connect LMs and how these connections change depending on the temperature change. The dependence of the dominant connections on the inclination parameter F is also examined.

1. Normal random potential: RFM of $F=0$

By using the Dijkstra algorithm, the dominant pathways coming into the GM are computed for RFM of $F=0$ with various temperatures. We observe 26 changes of dominant pathways by varying the temperature. Figure 5(a) is the SCG of the dominant pathways for high-temperature limit ($\beta \to 0$). This graph shows that 13 NDS, as well as many DS, links are chosen for the dominant paths. Since in the extreme case the energies are irrelevant for the route cost, these paths are actually the smallest transition-step pathways. At low temperatures, as depicted in Fig. 5(b), only NDSs with relatively low saddle energies are chosen as the shortest paths, thereby introducing the generic tendency that the shortest paths come to exist in the low-energy region and the number of NDSs, as a result, decreases as the temperature decreases. Note that, for the same number of NDSs, shortest path switching can occur, as exemplified by Figs. 5(b) and 5(c). In low-temperature limit, as expected, all the dominant paths are composed of the DSs. Comparing the DSs in Figs. 5(a) and 5(d), we see that the DSs in the fewest-step pathways [Fig. 5(a)] exist in the relatively high energy region.

2. Single funnel potential: RFM of $F=1.2$

We observe five changes of dominant pathways coming into the GM by varying the temperature. Since this potential has a single funnel character, there exists a pathway from each LM to the GM with disconnective saddles whose energies monotonically decrease. The existence of disconnective pathways excludes all NDSs as elements of dominant pathways except very short shortcut NDSs. Hence, as depicted in Fig. 6(a), even at high temperature, only five NDSs are used for dominant pathways, fewer than the normal random potential [13 NDSs in Fig. 5(a)]. We see that, as the temperature is decreased to $\beta=8.5$, no NDSs are used for dominant pathways [Fig. 6(c)].

3. Smooth funnel potential: RFM of $F=2.4$

For this very smooth funnel potential, the dominant pathways change only once. Even at high temperature, only one very short shortcut NDS is used for dominant pathways, as shown in Fig. 7(a) However, as the temperature is decreased, we see that the dominant pathways are composed of all DSs [Fig. 7(b)].

4. Dependence of dominant paths on F

To see how the switches of the dominant paths depend on temperature more closely, we plot the numbers of NDSs belonging to the shortest paths as functions of β for various F in Fig. 8. We see that for all RFMs the numbers of NDSs gradually decrease as the temperature is decreased. Furthermore, smoother funnel PESs result in more rapid decreases in NDSs. Note that, for $F=0$, a few NDSs remain very competitive even at rather low temperatures $\beta \sim 80$, where their

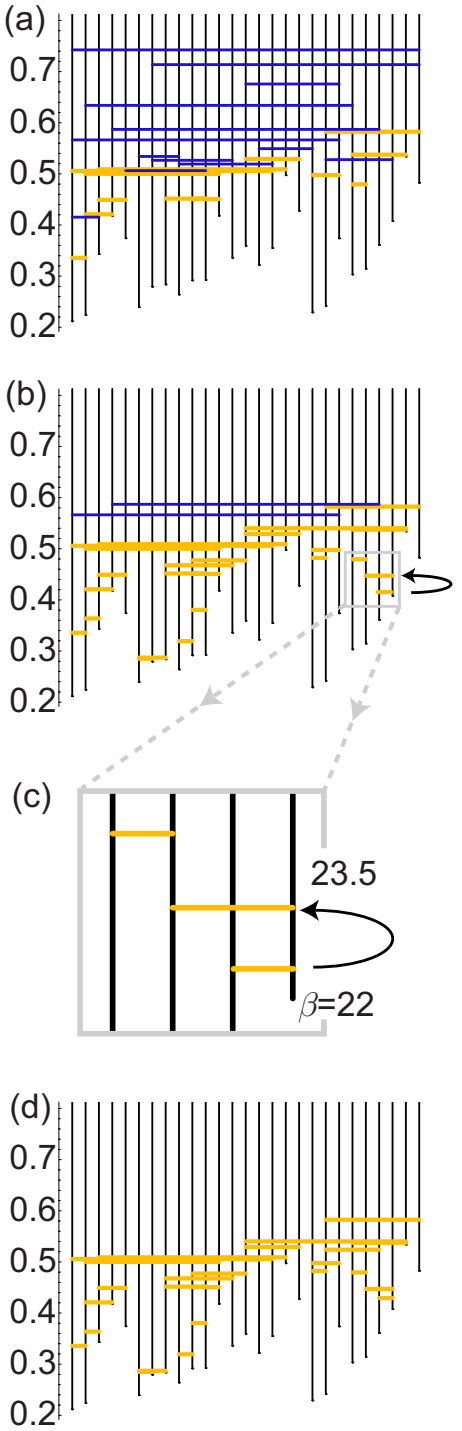

FIG. 5. (Color online) The dominant pathways of RFM with $F=0$ are represented in SCGs. (a) The SCG at $\beta=0$. (b) The dominant pathway switches between $\beta=22$ and 23.5 with the number of NDSs fixed. The dominant pathways at $\beta=22$ and 23.5 are superposed. (c) The blowup of the switch in (b). (d) The SCG at $\beta=79$. Here, the saddle lines are colored as in Fig. 3. All frequency factors ν_{ji} are set to 1 for simplicity.

energetic penalties are overcome because of being on the shortcuts to the GM. These suggest that NDSs become more competitive for many-dimensional systems, where a rich variety of energetically degenerative dynamical paths is introduced to the PESs.

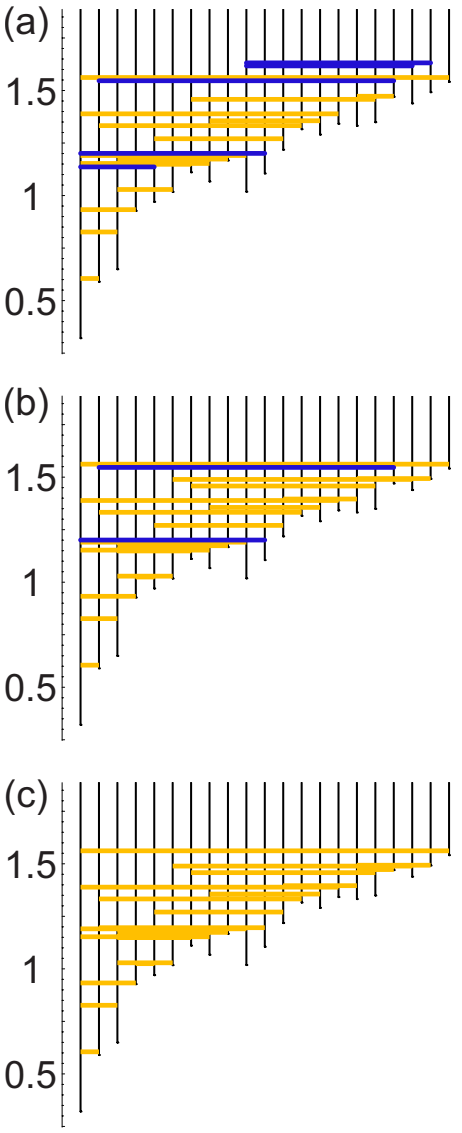

FIG. 6. (Color online) The dominant pathways for RFM of $F=1.2$ are represented in SCGs for (a) $\beta=0$, (b) 5, and (c) 8.5, where the saddle lines are colored as in Fig. 3. All frequency factors ν_{ji} are set to 1 for simplicity.

V. COARSE-GRAINING METHOD FOR SCG

When we try to apply SCG to a realistic multidimensional system, a well-known difficulty in visualization of DG arises also in SCG due to the high dimensionality of such a realistic PES. Namely, the huge number of LM lines makes the structure of the PES difficult to perceive. A number of coarse-graining methods for DG, such as lowest minima truncation, the monotonic sequence method with minima, the catchment basin transformation, and a procedure of low-barrier grouping, have been used [1,22,29,38–40].

In this section, we develop a monotonic sequence scheme that groups *saddle sequences* with increasing flow as a

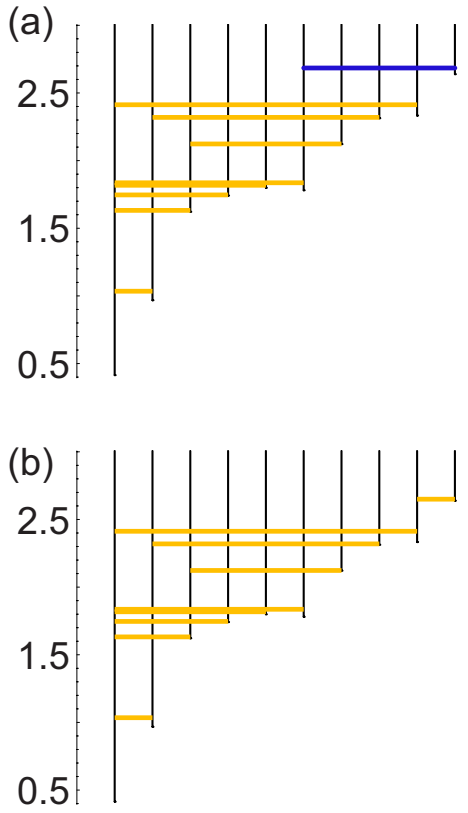

FIG. 7. (Color online) The dominant paths for RFM of $F=2.4$ are represented in SCGs for (a) $\beta=0$ and (b) 6.5, where the saddle lines are colored as in Fig. 3. All frequency factors ν_{ji} are set to 1 for simplicity.

coarse-graining method for our SCG. As shown in the following, this procedure is a coarse-graining method tailored for extracting the kinetic properties of the system.

A. Monotonic sequence method

We construct the coarse-graining map ϕ for LMs,

$$L_i \mapsto L'_{i'} \quad \text{with} \quad i' = \phi(i), \tag{20}$$

where $L'_{i'}$ denotes the coarse-grained LM of the i'th smallest energy. As described below, ϕ is composed of two mappings:

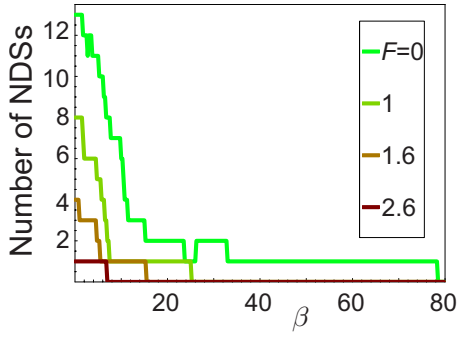

FIG. 8. (Color online) The numbers of NDSs on the dominant pathways are plotted as a function of β for $F=0,1,1.6,2.6$. All frequency factors ν_{ji} are set to 1 for simplicity.

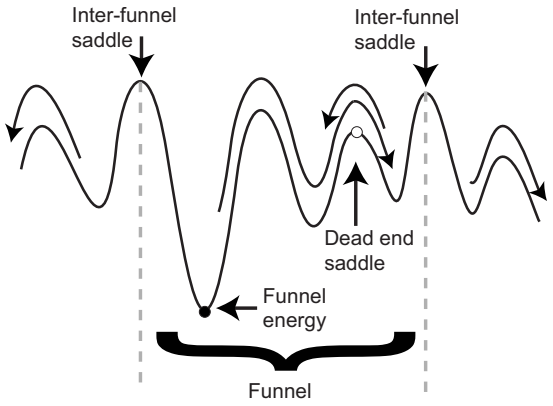

FIG. 9. 1D example of coarse graining with the monotonic sequence method. The arrowed curves represent the monotonic sequences. The open circle is a dead-end saddle [S_b in Eq. (21)]. The underbrace is the basin of the monotonic sequence mapping [Eq. (22)], which defines the funnel. The funnel energy [Eq. (23)] is represented by the solid circle. The interfunnel saddles are indicated by down arrows. The other saddles are intrafunnel saddles (see text).

$\phi=\chi\circ\varphi$, where φ and χ are, respectively, the contraction of LMs and the sorting of the contracted LMs in the increasing order of their energies.

The contracting map φ is given by the monotonic sequences. As depicted in Fig. 9, in each iteration of this algorithm a saddle search is performed in the direction of the least cost, namely, the maximum flow, at the current LM

$$L_a \mapsto S \mapsto L \mapsto \cdots \mapsto S_b, \tag{21}$$

where the dead-end saddle S_b is easily detected in computation by the coincidence of saddles in two successive transitions. Note that, if all frequency factors are uniform, the maximum flow saddle is identical with the lowest-energy saddle at each LM. Nonuniform saddle frequencies, in contrast, can result in temperature-dependent funnel decompositions.

In this way, one obtains the monotonic sequence map

$$a \mapsto b = \varphi(a). \tag{22}$$

The monotonic sequence basin $\varphi^{-1}(b)$ is the funnel labeled by b and all LMs are classified into all the funnels. The energy of funnel is defined by the lowest energy of $\varphi^{-1}(b)$, i.e.,

$$\min\{E_a^{\mathrm{LM}} | L_a \in \varphi^{-1}(S_b)\}. \tag{23}$$

Then, the funnel energies are sorted in an ascending order and the position at which S_b appears in the ordered list is denoted by $\chi(b)$.

Lastly, by identifying the funnels with the coarse-grained LMs, these procedures define the coarse-graining map

$$L_i \mapsto L'_{i'}, \tag{24}$$

$$i' = \chi \circ \varphi(i) \equiv \phi(i), \tag{25}$$

$$E_{i'}^{\mathrm{LM}'} = \min\{E_i^{\mathrm{LM}} | i \in \phi^{-1}(i')\}. \tag{26}$$

Accordingly, the saddle connectivity is also coarse grained as

$$\phi \circ g(S_j) = \{\phi(j_1), \phi(j_2)\},$$

where Eq. (1) is used. Here, S_j with $\phi(j_1) \neq \phi(j_2)$ are interfunnel saddles, while the others are intrafunnel saddles. The interfunnel saddle energies are sorted in an ascending order and the position at which the energy of S_j appears in the ordered list is denoted by $\psi(j)$, similar to the treatment of LMs. The intrafunnel saddles S_j are, for convenience, defined to be mapped to $j' = \psi(j) = 0$.

In this way, one obtains the coarse-graining map for SPs as follows:

$$S_j \mapsto S'_{j'}, \tag{27}$$

$$j' = \psi(j), \tag{28}$$

$$E_{j'}^{\mathrm{SP}'} = E_j^{\mathrm{SP}}, \tag{29}$$

$$g'(S'_{j'}) = \phi \circ g(j) \quad \text{for } j' \geq 1, \tag{30}$$

$$\psi^{-1}(j' = 0) = \{\text{intrafunnel saddles}\}. \tag{31}$$

The coarse-grained $E_{i'}^{\mathrm{LM}'}$, $E_{j'}^{\mathrm{SP}'}$, and g' [Eqs. (26), (29), and (30), respectively] provide the complete data for generating the coarse-grained SCG. The intrafunnel saddles (31) disappear from the coarse-grained SCG and, in other words, are confined into the microscopic level of description introduced via the monotonic sequence method. Note that the saddle characters of disconnectiveness or nondisconnectiveness [Sec. II C] are inherited via this coarse graining, because the above monotonic sequence method preserves the sequential order of the saddle energies.

Furthermore, on the basis of the approximate rate formula (14), we see that the coarse-grained saddles take lots of time for transition, compared to the intrafunnel saddles, in the course of wandering among a number of funnels. Hence, the above-mentioned coarse-graining method not only is a grouping method that is useful to simplify complicated graphs but also is a method for extracting the rate-limiting principal saddles.

B. Iterative use of the coarse graining for extracting hierarchal connection in PES

By iteratively applying this coarse-graining scheme to $\{E_i^{\mathrm{LM}_1}\} \equiv \{E_i^{\mathrm{LM}}\}$, $\{E_j^{\mathrm{SP}_1}\} \equiv \{E_j^{\mathrm{SP}}\}$, $g_1 \equiv g$, one obtains a series of coarse-grained SCG data $\{E_i^{\mathrm{LM}_2}\} \equiv \{E_i^{\mathrm{LM}'}\}, \{E_j^{\mathrm{SP}_2}\} \equiv \{E_j^{\mathrm{SP}'}\}, g_2 \equiv g', \ldots$, until it contains only one LM at $n = n_{\max} + 1$, i.e., $\{E_j^{\mathrm{LM}_{n_{\max}+1}}\} = \{E_{\mathrm{G}}^{\mathrm{LM}}\}$. Hence, we obtain the coarse-grained SCG data

$$(\{E_i^{\mathrm{LM}_1}\}, \{E_j^{\mathrm{SP}_1}\}, g_1), (\{E_i^{\mathrm{LM}_2}\}, \{E_j^{\mathrm{SP}_2}\}, g_2), \ldots,$$
$$(\{E_i^{\mathrm{LM}_{n_{\max}}}\}, \{E_j^{\mathrm{SP}_{n_{\max}}}\}, g_{n_{\max}}).$$

Using these coarse-grained data, we obtain the coarse-grained graphs, $\mathrm{SCG}_1, \mathrm{SCG}_2, \ldots \mathrm{SCG}_n, \ldots \mathrm{SCG}_{n_{\max}}$, describing the connection among coarse-grained funnels at macroscopic levels specified by n.

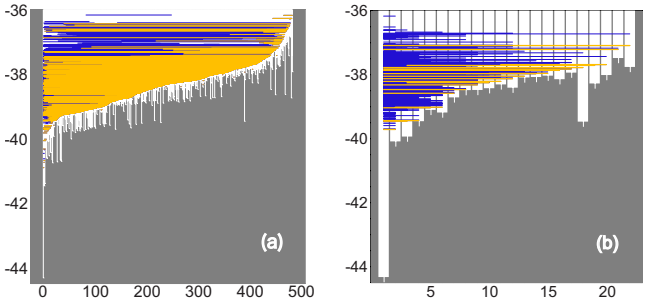

FIG. 10. (Color online) All of the saddle connections are depicted in SCG for 13-atom LJ cluster, where the saddle lines are colored as in Fig. 3. The vertical axes are stationary point energies in unit of ϵ and the horizontal axes are the numbers of LM locations. (a) SCG_1: LM lines are drawn in white against the black background to make them easier to see. (b) SCG_2 gives a simplified description. The structure is a single funnel potential (see text).

VI. APPLICATION TO REALISTIC SYSTEMS: LENNARD-JONES CLUSTERS

In this section, we show the SCGs of 13- and 38-atom LJ clusters, illustrating the applicability to realistic multidimensional systems. First, we discuss the structures of their saddle connectivity via SCG visualization at various coarse-graining levels of description. Then, we examine the mean first passage time statistics, confirming that gradual changes from liquid to solid phase occur when lowering temperature in each cluster. Finally, we show, with the use of SCG visualization, that the observed gradual changes result from the switches of dominant transition pathways at various macroscopic levels.

A. Structures of LJ clusters

The Lennard-Jones (LJ) pair potential has the form

$$V(r) = 4\epsilon\left[\left(\frac{\sigma}{r}\right)^{12} - \left(\frac{\sigma}{r}\right)^{6}\right], \tag{32}$$

where r is the interparticle distance, ϵ is the depth of the potential well, and σ controls the equilibrium distance between the neighboring atoms. The distance at the minimum of the potential well is $2^{1/6}\sigma$. All quantities reported below are given in reduced units of ϵ, σ. (For argon, the parameters are fitted and the values are $\epsilon = 1.67 \times 10^{-21}$ J and $\sigma = 3.40$ Å.)

1. 13-atom LJ cluster

For the 13-atom LJ cluster, we use a stationary point database created via discrete pathway sampling method [25]. A connected set of about 500 LMs including the GM and the saddles connecting them is used for generating the SCG.

As shown in Fig. 10(a), there are too many LMs to distinguish individual lines in SCG_1. Hence, the coarse graining

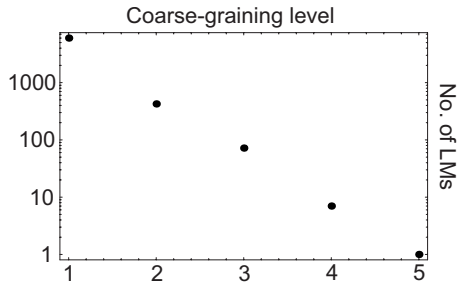

FIG. 11. For the 38-atom LJ cluster, the number of coarse-grained LMs is plotted as a function of coarse-graining level n. The number exponentially decreases until it becomes 1 at $n=5$.

procedure is iteratively applied to it. We confirm that the SCG reduces to a single vertical LM line at $n=3$ and thus $n_{\max}=2$. The PES structure is therefore decomposed into two levels: one is the macroscopic level consisting of the funnels and the interfunnel saddles ($n=2$) and the other is the microscopic level consisting of the intrafunnel LMs and the saddles connecting them ($n=1$).

Figure 10(b) shows the SCG_2 of LJ_{13}. The coarse-grained SCG has about 20 coarse-grained LMs. Hence, by the coarse graining, the LMs are contracted extensively, whose number is considerably decreased. Moreover, we see that the PES has the so-called "single funnel structure," where, from each coarse-grained LM of LM_2, there exists a transition pathway, to the GM, of disconnective interfunnel saddles with monotonically decreasing energies. Due to the single funnel character, the kinetically attracting LM of the terminal of all monotonic sequences agrees with the GM and thus relaxes in a methodical way to the GM. Note here that many NDSs connect coarse-grained LMs, as well as microscopic LMs. The role of NDSs for rate is examined later.

2. 38-atom LJ cluster

Also, here we use a stationary point database of LJ_{38} constructed in Ref. [25]. For the 38-atom LJ cluster, as shown in Fig. 11, the number of coarse-grained LMs exponentially decreases as the coarse-graining procedure is repeated. The SCG reduces to one vertical LM line at $n=5$ and thus the PES structure turns out to be composed of four layers: $n_{\max}=4$.

Figures 12(a) and 12(b) show the SCG_3 and the SCG_4 of LJ_{38}, where all saddles, both of disconnective and of nondisconnective connections, are depicted. As in the LJ_{13} case, many nondisconnective, as well as disconnective, saddles connect coarse-grained LMs at various macroscopic layers.

In contrast to the case of LJ_{13}, the SCG_4 in Fig. 12 shows that maximum flux pathways, of monotonically decreasing DSs in this case, reach the second lowest coarse-grained LM and start to move back and forth with the third LM from the left, which forms a kinetic trap at low temperature [the up arrow in Fig. 12(b)]. To reach the GM, the system must break away from the trap, next climbing the DS connecting L_1 and L_2. In this sense, the PES has the so-called "double funnel structure" [22,41,42], with antifocusing character [1].

B. Mean first passage time

We examine the mean first passage times, from the GMs to the other LMs, as an indicator of the dynamic properties

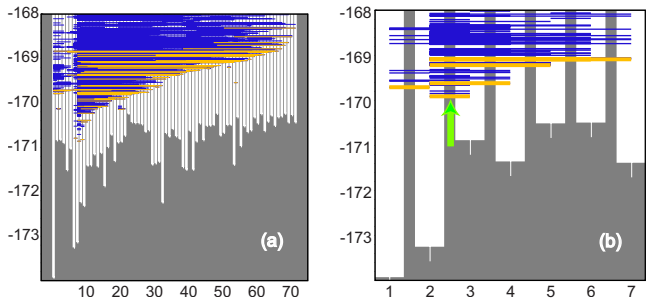

FIG. 12. (Color online) All of the saddle connections are depicted in coarse-grained SCGs (a) and (b) for LJ_{38}, where the saddle lines are colored as in Fig. 3. The vertical axes are stationary point energies in unit of ϵ and the horizontal axes are the numbers of LM locations. (a) SCG_3: LM lines are drawn in white against a black background. (b) SCG_4: a simpler description of the PES. The kinetic trap at low temperature is indicated by the arrow. The structure of this cluster is classified as a double funnel potential (see text).

on the PESs. Let us recall that, with the use of the total cost $C(i)$ of Eq. (18), the mean first passage time from the GM to L_i along the dominant pathway is given by

$$\tau(i) = C(i)e^{-\beta E_G^{LM}} Z_G(\beta), \tag{33}$$

under the same assumption of single dominance of transition pathways. Here, E_G^{LM} is the energy of GM. The expression for $C(i)$ in terms of the Dijkstra algorithm is given in Appendix D. Then, $\{\tau(i)|i=1,2,\ldots\}$ is sorted in order of arrival and the nth element is denoted by τ_n. The resulting τ_n shows the number of LMs found after a finite time evolution of dynamics.

Figure 13(a) shows τ_n as a function of n in high-temperature limit. Note here that the frequency factors are set to 1, for the sake of the computational simplicity. We see that all LMs of LJ_{13} in the figure are accessed from the GM in four time steps. This implies that these LMs are topologically connected to the GM by pathways of at most four steps and more importantly such pathways dominate in actual dynamics in high-temperature limit. Therefore, the dynamical state can be said to be in a liquid phase in which the system can travel quickly between any pair of LMs within several steps.

For LJ_{38}, in Fig. 14(a), we plot τ_n as a function of n, at $\beta=0$, where the frequency factors are also set to 1. We see that all LMs of LJ_{38} in the figure are accessed from the GM within more than a dozen time steps. Moreover, viewing this as the graph of LM number n found within the waiting time τ, we see that n increases exponentially with τ except near the very end at $n>5000$. This implies that LMs are found one after another at a constant rate as τ passes. Here, the system can travel between any pair of LMs within at most dozens of time steps, which shows again that the dynamical state is in a liquid phase.

In the low-temperature region, transition times needed for going over saddles exponentially grow as the temperature decreases. For this reason, we introduce the marginal passage time $\delta\tau_n$, which is defined by the additional average time for finding one extra LM, and further convert it to the reduced

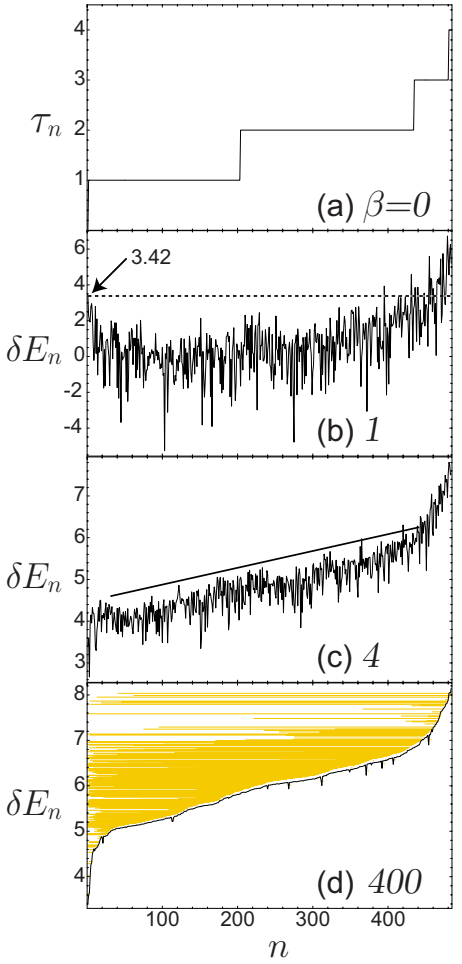

FIG. 13. (Color online) The mean first passage times τ and the reduced energy gaps δE in unit of ϵ of the LJ_{13} cluster. (a) The passage times τ_n at β=0 are plotted as a function of the order n of arrival. All frequency factors ν_{ji} are set to 1. The reduced energy gaps δE_n are plotted as functions of n for (b) β=1, (c) 4, and (d) 400. For eye guidance, δE_n=3.42 is plotted (dashed line) in (b); in (c) the bold line shows the approximate linear increase in δE_n. All DSs are also shown with energy shifted by $-E_G^{LM}$ in (d).

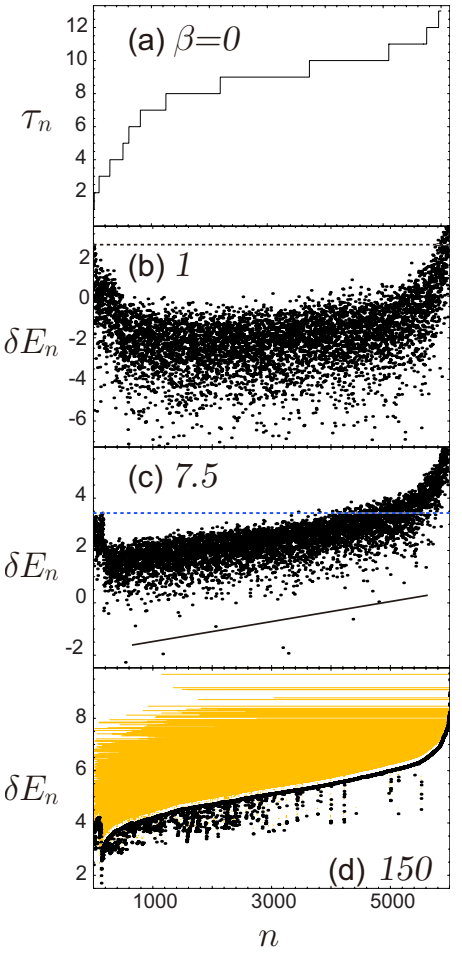

FIG. 14. (Color online) The mean first passage times τ and the reduced energy gaps δE in unit of ϵ of the LJ_{38} cluster. (a) The passage times τ_n at β=0 are plotted as a function of the order n of arrival. All frequency factors ν_{ji} are set to 1. The reduced energy gaps δE_n are plotted as functions of n for (b) β=1, (c) 7.5, and (d) 150. For eye guidance, δE_n=2.4 is plotted (dashed line) in (b). All DSs are also shown with energy shifted by $-E_G^{LM}$ in (d) (see text).

energy gap δE_n in order to extract useful information from the changes observed at various temperatures,

$$\delta\tau_n = \tau_n - \tau_{n-1}, \quad \delta E_n = \frac{\ln \delta\tau_n}{\beta}. \tag{34}$$

See Appendix D for the expression for $\delta\tau_n$ in terms of the Dijkstra algorithm.

Figures 13(b)–13(d) show the effective energy gaps δE_n of LJ_{13} at various temperatures. Figure 13(b) shows δE_n as a function of n at β=1. Starting from $\delta E_1 = \min\{E_j^{SP} | S_j = \text{adjacent to GM}\} - E_G^{LM} = 3.42052$, it ranges from −4 to 6. Almost all LMs up to $n \sim 400$ are found one after another at tiny time intervals, corresponding to very small energy gaps. In this case too, therefore, the state is a liquid phase.

At a relatively low temperature β=4, in contrast, the effective gaps increase as shown in Fig. 13(c). Especially, around from n=100 to 400 the tendency fits approximately to a line, implying that the marginal passage time for finding one extra LM increases exponentially as time passes: $\delta\tau_n \sim \exp[\beta(an+b)]$ with constants a and b. In low-temperature limit, the effective gaps converge to a curve as shown in Fig. 13(d). Moreover, it shows that the limiting curve is in accordance with the lower envelope of disconnective saddles, which is natural because, in such a low-temperature region, NDSs—being energetically more expensive than the disconnective ones—are not allowed any more.

Next, we plot the effective energy gaps of LJ_{38} in Figs. 14(b)–14(d). In high-temperature region (β=1), LMs up to n=5000 are found one after another at tiny time intervals, corresponding to very small energy gaps, ranging from −2 to −7, as shown in Fig. 14(b). In this case too, the state is a liquid phase. In contrast, Fig. 14(c) shows that at a relatively low temperature (β=7.5) the high-energy gaps of $\delta E \sim 3$ appear from n=1 to ~200 and then the small gap region widely spreads up to about n=4000. Hence, once having climbed over the high-energy gap region, the state suddenly spreads over the small gap region. In the low-temperature limit, the LM of $\delta E \sim 0$ at $n \sim 180$ corresponds to the second

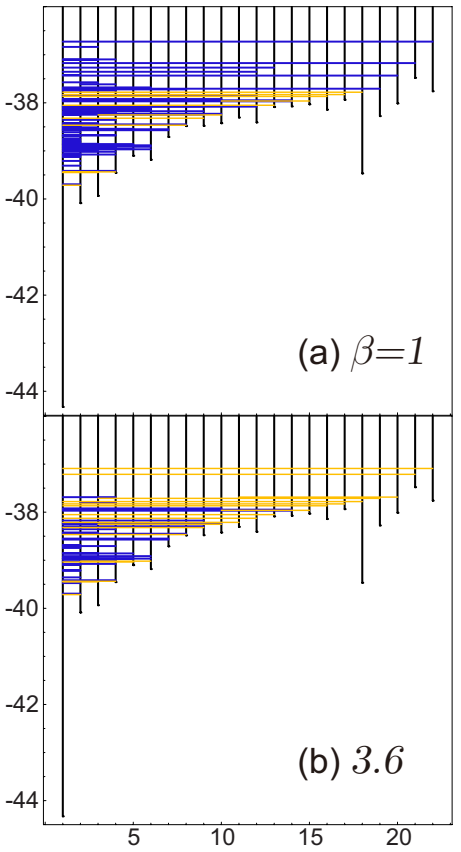

FIG. 15. (Color online) The dominant paths for LJ_{13} are represented in SCG_2 at (a) $\beta=1$ and (b) 3.6. The vertical axes are stationary point energies in unit of ϵ and the horizontal axes are the numbers of LM locations. Here, the saddle lines are colored as in Fig. 3. All frequency factors ν_{ji} are set to 1.

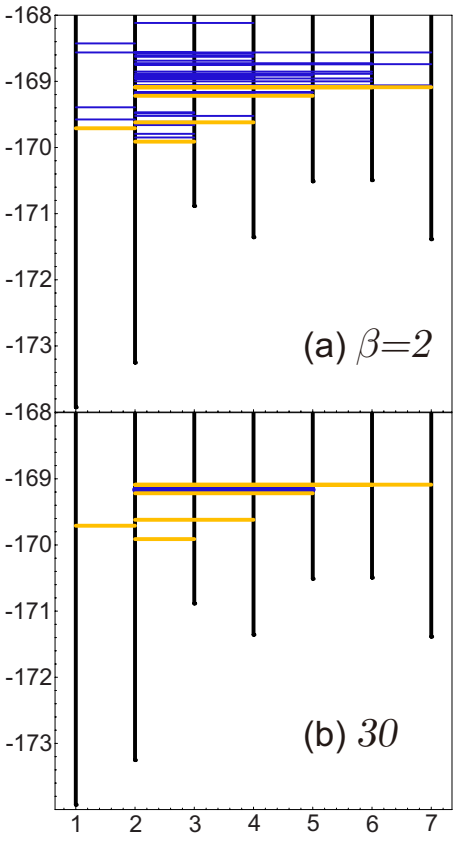

FIG. 16. (Color online) The dominant paths for LJ_{38} are represented in SCG_4 at (a) $\beta=2$ and (b) 30. The vertical axes are stationary point energies in unit of ϵ and the horizontal axes are the numbers of LM locations. Here, the saddle lines are colored as in Fig. 3. All frequency factors ν_{ji} are set to 1.

lowest icosahedral conformer and, as in LJ_{13}, the limiting curve is in accordance with the lower envelope of disconnective saddles, as illustrated in the $\beta=400$ case [Fig. 14(d)].

C. Saddle connectivity graph analysis for dominant pathways

We have observed the temperature-dependent switches of dominant pathways that carry the maximum probability currents, confirming that the dominant pathways change from the fewest-step pathway (i.e., maximum frequency pathways) to the smallest energy pathways, as temperature is lowered. The question addressed here is how the dominant pathways are determined by dynamics between the limiting temperatures. To elucidate this, we study the pathway changes at intermediate temperature by using SCG visualization at the most macroscopic level ($n=n_{\max}$) for each cluster.

In Fig. 15, the most dominant pathways of LJ_{13} from the GM, at $\beta=1$ [Fig. 15(a)] and 3.6 [Fig. 15(b)], are shown in second-order coarse-grained SCGs. Figure 15(a) shows that at high temperature great many NDSs, as well as DSs, are utilized to link coarse-grained LMs together. Namely, at the temperature, many microscopic LMs contained in coarse-grained LMs are directly connected by NDSs. This is consistent with the above observation that at high temperature pathways are routed on the fewest-step principle because, for connecting all LMs to the GM within a few steps, the system has to utilize not only disconnective but also many shortcut nondisconnective saddles even at the macroscopic level.

As shown in Fig. 15(b), at relatively low temperature the number of NDSs on the dominant paths is decreased. Especially, all dominant pathways from the right LMs (at around 15–20) become disconnective. Due to the funnel character of LJ_{13}, LMs to the right in SCG_2 are connected with relatively high energy saddles. These high-energy saddles, except indispensable DSs, soon become unused with lowering temperature. Hence, at low temperature, almost all dominant pathways are disconnective and only energetically competitive NDSs, which are at around the bottom of the funnel, can be dominant. This is qualitatively equivalent to the result of RFM in the case of the smooth funnel $F=2.4$ in Sec. IV D 3.

Figure 16 shows the dominant pathways of LJ_{38} at $\beta=2$ [Fig. 16(a)] and 30 [Fig. 16(b)] in the most macroscopic SCG_4. At high temperature, as shown in Fig. 16(a), many NDSs are dominant, as in Fig. 15(a). Even at low temperature, in contrast, competitive NDSs exist due to the multifunnel structure of LJ_{38}, as illustrated in Fig. 16(b). Here, we again confirmed that the antifocus character of multifunnel structure results in the multiplicity of dominant pathways surviving at low temperature. In summary, we confirmed with the use of SCGs that the dominant pathways of LJ

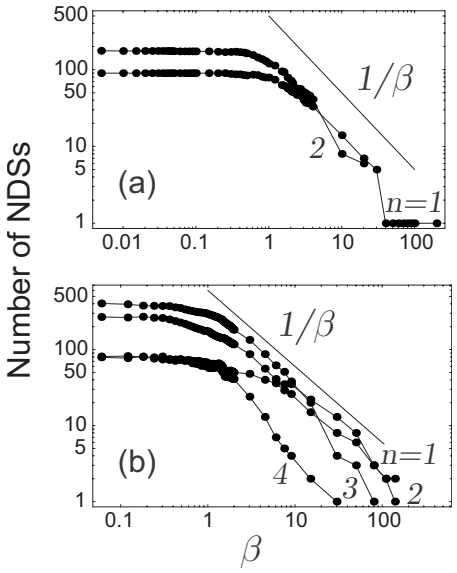

FIG. 17. The numbers of NDSs belonging to the nth macroscopic level on the dominant pathways are plotted as functions of β in unit of ϵ^{-1} for (a) LJ_{13} and (b) LJ_{38}. For eye guidance, the lines of $\propto 1/\beta$ are also plotted (see text).

clusters switch with temperature change even at most macroscopic levels and that the changes are qualitatively equivalent to those of RFMs observed in Sec. IV D, although they differ in system sizes.

D. Saddle hierarchy in dominant pathways

The pathway switches observed at the most macroscopic levels suggest that many more nondisconnective to disconnective switches occur in microscopic interfunnel saddle connections. Hence, we count how many NDSs are used for dominant pathways at each macro-micro hierarchy level. We classify the saddles into n levels $(n=1,2,\ldots,n_{\max})$ by the following: if a saddle connects nth coarse-grained LMs but does not connect $(n+1)$th coarse-grained LMs, we call it a nth level saddle. In other words, nth saddles are components exclusively of nth coarse-grained funnels and, therefore, appear in $SCG_1, SCG_2, \ldots, SCG_n$ and disappear from SCG_{n+1}.

Figures 17(a) and 17(b) show the numbers of nth-order NDSs in dominant pathways to the GMs as functions of β for LJ_{13} and LJ_{38}, respectively. In both figures, we see that the plots share a common feature that, in high-temperature region $\beta<1$, the numbers are approximately constant values, while as temperature is lowered they decease as $\sim 1/\beta$. Namely, the dominant pathways are chosen in a self-similar way at different levels from microscopic to macroscopic scales.

Note that the self-similarity is confirmed both in 13- and in 38-atom clusters. This suggests that the observed self-similarity is a universal pair-potential property independent of the size of clusters.

VII. CONCLUDING REMARKS

In this paper, we have developed a topographic representation of PES, called SCG, and the usefulness of our method is also demonstrated by applying it to realistic Lennard-Jones clusters. As shown in Sec. II, the SCG is a generalized DG, which is extended to include dynamically dominant NDSs, as well as static statistically dominant DSs. With this graph, we have confirmed that the dynamically dominant pathways are frequently switched with temperature change by studying the kinetics of Markovian basin hopping on two-dimensional RFM. The RFM is an illustrative funnel potential introduced in Sec. III.

In Sec. IV, we developed an efficient method to systematically compute all of the dominant pathways, with the help of Dijkstra's shortest path algorithm. Especially, with the use of the 2D RFMs of various funnel inclination parameters, we computed the numbers of NDSs on the dominant pathways as an indicator of the multiplicity in the saddle connection on PES and elucidated the general relation between the multiplicity and the funnel smoothness.

In Sec. V, the coarse-graining method for our SCG was constructed with the use of the monotonic sequence method. This method identifies macroscopic LMs as funnels of LMs, with the use of terminal saddles of most probable pathways. This coarse-graining method not only reduces the graphical complexity, but also enables us to extract the hierarchical structures in saddle connectivity by iterative use.

By using these methods, in Sec. VI, we elucidated that the change in passage time statistics with temperature change depends on the dominant pathway switches for 13- and 38-atom LJ clusters. The analysis is based on the data determined in Ref. [25]. Macroscopically, the properties of dominant pathways of realistic potentials can be qualitatively understood by the analogy of the simple RFM with suitable inclination parameters. At each hierarchical level, moreover, the self-similar power-law dependency of dominant NDSs on temperature was revealed. The self-similar dependency was suggested to be common in the same pair-potential clusters. These show that our methods provide us a sound basis for understanding the multiple connections in dynamics and structures on the complex many-dimensional PESs.

Note that, for the sake of computational simplicity, we set all frequency factors to be 1 in this paper. Of course, the SCG visualization, the Dijkstra algorithm for dominant pathways, and the monotonic basin coarse graining are applicable to the case of varying frequency factors. However, in this case, monotonic sequences may depend on the temperature and thus monotonic sequence basins can change with temperature change. For example, let a LM have two saddles, S_1 and S_2, of energies E_1 and E_2 $(E_1<E_2)$, respectively, with frequency factors ν_1 and ν_2 $(\nu_1<\nu_2)$. At low temperature S_1 is dominant, while at high temperature S_2 is dominant. Namely, the most probable path from the LM changes from S_1 to S_2 with raising temperature.

In summary, in order to overcome the difficulty in understanding thermodynamic and kinetic properties on complicated potential-energy surfaces, we presented a visualization procedure, called saddle connectivity graph. This graph method is applicable to analyzing the kinetics of systems with complex potential-energy landscapes. We demonstrated the effectiveness of the method for realistic systems, by applying it to the coarse-grain analysis of Lennard-Jones clusters with a coarse-graining procedure. The coarse-graining

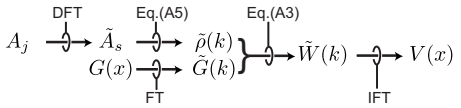

FIG. 18. The flowchart of a Fourier-based computation for RFM $V(x)$. DFT means the discrete Fourier transform of Eq. (A1), FT means the Fourier transformation (A4), and IFT means the inverse Fourier transformation (A2).

method revealed self-similar hierarchical structures, which are common to many-atom Lennard-Jones clusters. We expect that these methods will help us to promote our understanding of kinetics on realistic complex potential surfaces.

ACKNOWLEDGMENTS

The authors acknowledge and express their gratitude to D. J. Wales for permitting the use of LJ data of the minima and transition states [25] and to S. Tsuji for his hospitality in providing a location for our discussions. This work was supported by Grants-in-Aid for Scientific Research on Priority Areas (2) Grants No. 14077213 and No. 14077220 from the Ministry of Education, Culture, Sports, Science and Technology of Japan.

APPENDIX A: COMPUTATION OF RANDOM FUNNEL MODEL

In this part, we describe the computational method for RFM potential introduced in Sec. III. First, for the computation of 1D RFM potential $V(x)$, we proceed as follows. We first set A_j at uniformly distributed random numbers in the range of 0–1 for $j=1,2,\ldots,L$, then translate it under the periodic condition so that the minimum of A_j is located at the center $j=L/2$, and redefine A_j by adding the prototype function $U(j)$ to A_j. The intermediate potential at this stage is represented by

$$W(x) = [G * \rho](x) = \sum_{n=-\infty}^{\infty} \sum_{j=1}^{L} A_j \frac{1}{\sqrt{2\pi}\sigma} e^{-(x-j-nL)^2/2\sigma^2},$$

where $*$ denotes convolution. Finally, RFM potential $V(x)$ is obtained via low-pass filtering of $W(x)$ with truncation wave number π.

Here, to efficiently compute the convolution with truncation, one can resort to Fourier-based techniques, as depicted in Fig. 18. Namely, we first evaluate the discrete Fourier transform of A_j as

$$\tilde{A}_s = \frac{\sqrt{2\pi}}{L} \sum_{j=1}^{L} A_j e^{-ik_s j}, \tag{A1}$$

with $k_s=2\pi s/L$ and then compute $V(x)$ via the following Fourier transformation:

$$V(x) = \int_{-\pi}^{\pi} \frac{e^{ikx}}{\sqrt{2\pi}} \tilde{W}(k) dk = \sum_{s=-L/2+1}^{L/2} e^{ik_s x} \tilde{G}(k_s) \tilde{A}_s, \tag{A2}$$

where the following identities are used:

$$\tilde{W}(k) = \sqrt{2\pi} \tilde{G}(k) \tilde{\rho}(k), \tag{A3}$$

$$\tilde{G}(k) = \frac{1}{\sqrt{2\pi}} \exp(-\sigma^2 k^2/2), \tag{A4}$$

$$\tilde{\rho}(k) = \sum_s \tilde{A}_s \delta(k - k_s). \tag{A5}$$

Note that the wave number in Eq. (A2) is in the allowed region $-\pi < k < \pi$.

Finally, we explain the computation of d-dimensional RFM potential $V(x_1,x_2,\ldots,x_d) \equiv V(\mathbf{x})$. Similarly to the 1D potential, $V(\mathbf{x})$ is efficiently evaluated via Fourier-based procedures. Namely, by using the discrete Fourier transform of $A_{\mathbf{j}}$,

$$\tilde{A}_{\mathbf{s}} = (\sqrt{2\pi}/L)^d \sum_{\mathbf{j} \in D} A_{\mathbf{j}} e^{-i\mathbf{k_s}\mathbf{j}} \tag{A6}$$

with $\mathbf{k_s}=2\pi\mathbf{s}/L$; $V(\mathbf{x})$ is computed by

$$V(\mathbf{x}) = \sum_{\mathbf{s}}{}' e^{i\mathbf{k_s}\mathbf{x}} \tilde{G}(\mathbf{k_s}) \tilde{A}_{\mathbf{s}}, \tag{A7}$$

where $\Sigma_{\mathbf{s}}' = \Sigma_{i=1}^{d} \Sigma_{s_i=-L/2+1}^{L/2}$ and

$$\tilde{G}(\mathbf{k}) = \frac{1}{(\sqrt{2\pi})^d} \exp\left(-\frac{\sigma^2}{2} \sum_{i=1}^{d} k_i^2 \right). \tag{A8}$$

APPENDIX B: EXPRESSION OF CANONICAL TRANSITION RATE

In the canonical RRKM theory, which is in fact equivalent to the transition state theory, the transition rate k_{ji} is given, at inverse temperature $\beta=(k_B T)^{-1}$ (k_B is the Boltzmann constant) by

$$k_{ji} = \frac{1}{\beta h} \frac{Z_j^{\dagger}(\beta)}{Z_i(\beta)} e^{-\beta(E_j^{\mathrm{SP}} - E_i^{\mathrm{LM}})}, \tag{B1}$$

where S_j is the saddle for the transition from L_i to L_j, $Z_j^{\dagger}(\beta)$ is the transition state partition function of S_j, and $Z_i(\beta)$ is the partition function of basin of minima L_i [43]. In harmonic approximation, the rate constant becomes

$$k_{ji} = \nu_{ji} e^{-\beta(E_j^{\mathrm{SP}} - E_i^{\mathrm{LM}})}, \tag{B2}$$

$$\nu_{ji} = \frac{1}{2\pi} \frac{\prod_{l=1}^{n} \sqrt{\lambda_l^{L_i}}}{\prod_{l=2}^{n} \sqrt{\lambda_l^{S_j}}}, \tag{B3}$$

where ν_{ji} is the frequency factor, n is the degrees of freedom, and λ_l^{P} ($l=1,2,\ldots$) is the lth smallest eigenvalue of the Hessian matrix

$$K_{ij} = \frac{\partial^2 V}{\partial x_i \partial x_j},$$

at a stationary point P [22].

APPENDIX C: DERIVATION OF EQS. (13) and (14)

We here describe the derivation of Eq. (14), according to Ref. [44]. In a steady state, the probability current J from L_a to L_b, along n-step pathway ℓ $(b \equiv i_n \leftarrow i_{n-1} \leftarrow \cdots \leftarrow i_2 \leftarrow i_1 \leftarrow i_0 \equiv a)$ obeys

$$J = k_{i_1,i_0} P_{i_0} - k_{i_0,i_1} P_{i_1}, \tag{C1}$$

$$J = k_{i_2,i_1} P_{i_1} - k_{i_1,i_2} P_{i_2}, \tag{C2}$$

$$J = k_{i_3,i_2} P_{i_2} - k_{i_2,i_3} P_{i_3}, \tag{C3}$$

$$\cdots$$

$$J = k_{i_n,i_{n-1}} P_{i_{n-1}} - k_{i_{n-1},i_n} P_{i_n}, \tag{C4}$$

where k_{i_m,i_n} is the rate from L_n to L_m. By summing Eq. (C1), (C2) $\times [k_{i_0,i_1}/k_{i_2,i_1}]$, (C3) $\times [k_{i_0,i_1}k_{i_1,i_2}/k_{i_3,i_2}k_{i_2,i_1}]$, $\ldots$, (C4) $\times [k_{i_0,i_1}k_{i_1,i_2}\cdots k_{i_{n-2},i_{n-1}}/k_{i_n,i_{n-1}}\cdots k_{i_3,i_2}k_{i_2,i_1}]$, one obtains

$$J = \frac{k_{i_1,i_0}P_{i_0} - \left(\prod_{m=1}^{n-1} \frac{k_{i_m,i_{m+1}}}{k_{i_{m+1},i_m}}\right) k_{i_{n-1},i_n} P_{i_n}}{1 + \frac{k_{i_0,i_1}}{k_{i_2,i_1}} + \frac{k_{i_0,i_1}k_{i_1,i_2}}{k_{i_3,i_2}k_{i_2,i_1}} + \cdots + \prod_{m=1}^{n-1} \frac{k_{i_m,i_{m+1}}}{k_{i_{m+1},i_m}}}.$$

Since an external sink and source are, respectively, connected to L_b and L_a, we set $P_{i_0}=P_a=1$, $P_{i_n}=P_b=0$. By using Eq. (6), one obtains Eq. (13). Substituting Eq. (B1) into Eq. (13), we finally obtain the expression of Eq. (14).

APPENDIX D: DIJKSTRA ALGORITHM FOR ROUTE COST (18)

The inverse Dijkstra algorithm works by iteratively updating two sets, Q_D and S_D, which store, respectively, the undecided and the decided LMs. At each iteration, moreover, the marginal cost $\delta C(i)$ of the undecided L_i, which is additional to the cost decided in the previous iteration, as well as the saddle $P(i)$, through which the shortest path leaves from L_i are maintained.

We start with

$$\delta C(i) = \begin{cases} 0 & \text{for } i = b \\ \infty & \text{for } i \neq b, \end{cases}$$

$$Q_D = \{1, 2 \ldots, M\},$$

$$S_D = \phi.$$

Then, the following iterative procedure is applied until Q_D becomes empty:

(1) Find the minimum $\delta C(i)$ in $i \in Q_D$, where $\delta C(i)$ and $P(i)$ become fixed.

(2) Accordingly, Q_D and S_D are, respectively, updated by dropping i from Q_D and appending i to S_D.

(3) The unsettled marginal costs are shifted as $\delta C(i') = \delta C(i') - \delta C(i)$ for $i' \in Q_D$.

(4) Find $L_{i'}$ that are connected to the just previously settled L_i via S_j. For each i', if $C_{\text{pair}}(i,i') < \delta C(i')$, then make replacements of $\delta C(i') = C_{\text{pair}}(i,i')$ and $P(i') = j$.

By using these results, the total cost $C(i)$ along the dominant pathway from a L_i to L_b is given by

$$C(i) = \sum_{k=1}^{S_D^{-1}(i)} \delta C[S_D(k)], \tag{D1}$$

where $S_D(k)$ is the kth element of the ordered set S_D and S_D^{-1} denotes the inverse of this mapping. The dominant pathway itself is easily traced by iteratively finding the next saddle and the next LM by using $P(i)$ until L_b appears.

Finally, with the use of Eq. (D1), the following simple relation holds for the marginal passage time $\delta\tau_n$ [See Eq. (34) for the definition]:

$$\delta\tau_n = \delta C[S_D(n)] \quad \text{for } n = 1, 2, \ldots. \tag{D2}$$

[1] R. S. Berry and R. Breitengraser-Kunz, Phys. Rev. Lett. **74**, 3951 (1995).
[2] J. P. K. Doye and L. Meyer, Phys. Rev. Lett. **95**, 063401 (2005).
[3] J. P. K. Doye, Phys. Rev. Lett. **88**, 238701 (2002).
[4] C. P. Massen and J. P. K. Doye, Phys. Rev. E **71**, 046101 (2005).
[5] M. Menon, A. N. Andriotis, D. Srivastava, I. Ponomareva, and L. A. Chernozatonskii, Phys. Rev. Lett. **91**, 145501 (2003).
[6] Y.-H. Kim, I.-H. Lee, K. J. Chang, and S. Lee, Phys. Rev. Lett. **90**, 065501 (2003).
[7] O. M. Becker and M. Karplus, J. Chem. Phys. **106**, 1495 (1997).
[8] S. V. Krivov, S. F. Chekmarev, and M. Karplus, Phys. Rev. Lett. **88**, 038101 (2002).
[9] P. G. Debenedetti and F. H. Stillinger, Nature (London) **410**, 259 (2001).
[10] S. Sastry, Nature (London) **409**, 164 (2001).
[11] I. Saika-Voivod, P. H. Poole, and F. Sciortino, Nature (London) **412**, 514 (2001).
[12] M. Goldstein, J. Chem. Phys. **51**, 3728 (1969).
[13] F. H. Stillinger and T. A. Weber, Phys. Rev. A **25**, 978 (1982); Science **225**, 983 (1984); F. H. Stillinger, *ibid.* **267**, 1935 (1995).
[14] R. A. Denny, D. R. Reichman, and J.-P. Bouchaud, Phys. Rev. Lett. **90**, 025503 (2003).
[15] B. Doliwa and A. Heuer, Phys. Rev. Lett. **91**, 235501 (2003).
[16] A. Heuer, Phys. Rev. Lett. **78**, 4051 (1997).
[17] B. Doliwa and A. Heuer, Phys. Rev. E **67**, 031506 (2003).
[18] L. Angelani, G. Parisi, G. Ruocco, and G. Viliani, Phys. Rev. Lett. **81**, 4648 (1998).
[19] H. W. Sheng, W. K. Luo, F. M. Alamgir, J. M. Bai, and E. Ma,

Nature (London) **439**, 419 (2006).
[20] M. Winterlich, G. Diezemann, H. Zimmermann, and R. Böhmer, Phys. Rev. Lett. **91**, 235504 (2003).
[21] D. J. Wales, M. A. Miller, and T. R. Walsh, Nature (London) **394**, 758 (1998); D. J. Wales and H. A. Scheraga, Science **285**, 1368 (1999).
[22] D. J. Wales, *Energy Landscapes* (Cambridge University Press, Cambridge, England, 2004).
[23] P. Garstecki, T. X. Hoang, and M. Cieplak, Phys. Rev. E **60**, 3219 (1999).
[24] M. Cieplak, S. Vishveshwara, and J. R. Banavar, Phys. Rev. Lett. **77**, 3681 (1996); M. Cieplak and T. X. Hoang, Phys. Rev. E **58**, 3589 (1998).
[25] D. J. Wales, Mol. Phys. **100**, 3285 (2002); **102**, 891 (2004).
[26] T. Okushima, T. Niiyama, K. S. Ikeda, and Y. Shimizu, Phys. Rev. E **76**, 036109 (2007).
[27] E. W. Dijkstra, Numer. Math. **1**, 269 (1959).
[28] S. Saito, M. Matsumoto, and I. Ohmine, *Advances in Classical Trajectory Methods* (JAI Press, Stamford, CT, 1999), Vol. 4, 105.
[29] J. P. K. Doye, M. A. Miller, and D. J. Wales, J. Chem. Phys. **111**, 8417 (1999).
[30] R. A. Olsen, G. J. Kroes, G. Henkelman, A. Arnaldsson, and H. Jónsson, J. Chem. Phys. **121**, 9776 (2004).
[31] G. Henkelman and H. Jónsson, J. Chem. Phys. **111**, 7010 (1999).
[32] G. Henkelman and H. Jónsson, J. Chem. Phys. **113**, 9978 (2000).
[33] J. M. Carr, S. A. Trygubenko, and D. J. Wales, J. Chem. Phys. **122**, 234903 (2005).
[34] N. Shida, Adv. Chem. Phys. **130**, 129 (2005).
[35] T. S. Grigera, J. Chem. Phys. **124**, 064502 (2006).
[36] P. Hänggi, P. Talkner, and M. Borkovec, Rev. Mod. Phys. **62**, 251 (1990).
[37] D. J. Wales, Int. Rev. Phys. Chem. **25**, 237 (2006).
[38] T. F. Middleton, J. Hernández-Rojas, P. N. Mortenson, and D. J. Wales, Phys. Rev. B **64**, 184201 (2001).
[39] M. A. Miller, J. P. K. Doye, and D. J. Wales, J. Chem. Phys. **110**, 328 (1999).
[40] Y. Levy and O. M. Becker, Phys. Rev. Lett. **81**, 1126 (1998).
[41] J. P. K. Doye, M. A. Miller, and D. J. Wales, J. Chem. Phys. **110**, 6896 (1999).
[42] M. A. Miller, J. P. K. Doye, and D. J. Wales, Phys. Rev. E **60**, 3701 (1999).
[43] H. Eyring, J. Chem. Phys. **3**, 107 (1935).
[44] H. Eyring and E. M. Eyring, *Modern Chemical Kinetics* (Reinhold, New York, 1963).